Received April 5, 2022, accepted April 24, 2022, date of publication May 3, 2022, date of current version May 11, 2022.

Digital Object Identifier 10.1109/ACCESS.2022.3172475

Dual-Band Class J Power Amplifier at 2.45 and 5.8 GHz for UAVs Communications

AINHOA MORALES-FERNANDEZ[1], MONICA FERNANDEZ-BARCIELA[1], (Senior Member, IEEE), FERNANDO ISASI-VICENTE[1], FERNANDO MARTIN-RODRIGUEZ[1], AND PAUL J. TASKER[2], (Fellow, IEEE)

[1]AtlanTTic Research Center, Universidade de Vigo, 36310 Vigo, Spain
[2]Cardiff School of Engineering, Cardiff University, Cardiff CF24 3AA, U.K.

Corresponding author: Monica Fernandez-Barciela (monica.barciela@uvigo.es)

This work was funded by the Ministerio de Ciencia e Innovación (MCIN)/Agencia Estatal de Investigación (AEI)/10.13039/501100011033 and by The European Regional Development Fund (ERDF) A way of making Europe, under grant TEC2017-88242-C3-2-R.

ABSTRACT A hybrid dual-band power amplifier (PA) prototype working at two Industrial, Scientific and Medical (ISM) bands, 2.4-2.5 GHz and 5.725-5.875 GHz, was designed for Unmanned Aerial Vehicles (UAVs) communication applications in Spain. Initially, two single-band PA prototypes centered at each band were designed to evaluate the single-band achievable RF performance. In all the PAs, the Gallium Nitride (GaN) Qorvo HEMT TGF2977-SM was used, as well as microstrip transmission lines technology. To achieve wideband, good linearity and efficiency, the PAs were designed in class J. The measured results for the dual-band PA prototype at the 2dB compression point at the lower and higher bands, respectively, are 14.8 dB and 11.2 dB of Transducer Power Gain (G_T), 35.7 dBm and 34.8 dBm of RF output power (Pout) and 59.2% and 43.5% of Drain Efficiency (η). At 3dB compression the respective lower and higher bands results are 37.9 dBm and 37 dBm of Pout and 73.9% and 55% of η.

INDEX TERMS Class J, dual-band, GaN, microwaves, power amplifier.

I. INTRODUCTION

Unmanned Aerial Vehicles (UAVs) play a significant role in a growing number of civil applications. These aircraft require wireless and energy efficient communications to extend, as much as possible, the time between battery recharges. Consequently, 2.45 and 5.8 GHz Industrial, Scientific and Medical (ISM) bands are often used, since many wireless standards work in these bands, such as Bluetooth or WiFi. However, operating at two or more bands using the same transmitter with good RF performance at all bands without reconfiguration is a challenge. Moreover, since the PA is the most power consuming stage in the communications transceiver, good efficiency will be a requirement for a dual-band PA. High bandwidth and linearity are also desirable in this case, hence, the selection in this work of class J as a compromise to achieve all these design goals.

Several previously reported works on hybrid dual-band Gallium Nitride (GaN)-based PAs are included in table 1.

TABLE 1. Comparison of state-of-the-art dual-band PAs using GaN HEMTs.

Year / Ref	Frequency [GHz]	Pout [dBm]	PAE [%]	Technology / Transistor
2011 / [1]	1.5 / 3.8	37.3 (P3dB) / 35.7 (P1.5dB)	47 (P3dB) / 52 (P1.5dB)	Microstrip NPTB00004
2017 / [3] *	0.8 / 2.8	39.7 / 39.8	56 / 61	Microstrip CGH40010F
2017 / [4] *	2.4 / 5.8	41 / 36.7	55 / 36	SWI CGH40010
2019 / [5] *	2.1 / 5	$\approx$ 45 / $\approx$ 40	$\approx$ 70 / $\approx$ 45	Microstrip CGH40025F
2022 / This work	2.45 / 5.8	37.9 / 37	71 / 50	Microstrip TGF2977-SM

* simulated results

In [1] a dual-band PA was designed centered at 1.5 and 3.8 GHz, and operating at different classes at each band. Due to the difficulties they found when using the same matching networks for both bands, the biasing network at the higher band was used to aid matching at the

The associate editor coordinating the review of this manuscript and approving it for publication was Tae Wook Kim.

lower band, where class AB was used. To achieve class J matching at the upper band, a technique based on a previous approach [2], was introduced. Another class J dual-band PA was designed in [3], operating at the center frequencies of 0.8 and 2.8 GHz. The Output Matching Network (OMN) consists of crossed microstrip transmission lines, designed using the transformation of two-section transmission line, matching the fundamental and second harmonic impedances at both frequencies. But only simulation results were presented. The same occurs in [4], where the designed dual-band PA uses the same frequency bands as in this work and only lower-band measured performance is shown. It uses Substrate Integrated Waveguide (SIW) technology, instead of microstrip transmission lines. In [5] is presented a dual-band PA designed with the aim of preserving linearity and high efficiency. It employs 2.1 and 5 GHz as the center frequencies of each band and makes use of a matching procedure in two steps, which consists of matching at first complex to real impedances and then, real to real impedances.

In [6] is presented a concurrent class J PA working at closer bands than this work, 1.842 and 2.655 GHz. The matching networks were designed for matching the harmonic impedances and the impedance for the second order intermodulation, which was relevant to obtain good efficiency. The measured efficiency achieved in concurrent mode reaches 60% and the RF output power (Pout) exceeds 40 dBm at both center frequencies. More recently, in [7] the authors introduced a microstrip matching network designed as a combination of T and Π networks for working at 1.57 and 2.44 GHz. It also only includes simulation results. In [8], is presented a concurrent hex-band PA, which includes the two frequency bands selected for this work. Despite operating in more than two bands, at 2.5 and 5.8 GHz efficiency barely reached 41% and 20% Power Added Efficiency (PAE), respectively. Furthermore, a frequency shift was observed in the frequency bands above 4 GHz.

Other recent works which pursuit high efficiency, present class F PAs ([9] and [10]) with the corresponding harmonic control and, in the case of [9], proposed the use of a bandwidth expansion network. In [11] the transistor is biased in deep class AB and, to achieve high efficiency, the second harmonic impedances are selected with arbitrary values near open or short circuit. In [12], a dual-band coupler is proposed for the drain dual-band harmonic control and matching, and was demonstrated in lower frequency PAs.

Despite presenting good RF performance, most of these previous works operate at lower fundamental frequencies or at closer bands than the PA proposed in this work.

In next sections, a highly efficient dual-band class J* PA in hybrid microstrip technology, working at ISM bands 2.45 and 5.8 GHz, is described. To pre-evaluate the expected RF performance at each band, initially two single-band PAs were developed. PAs design, simulations and E-M optimizations were performed using Advanced Design System (ADS). Qorvo TGF2977-SM GaN HEMT was employed in all cases. Modelithics components models were used.

II. PA DESIGN

A. CLASS J OPERATION

The PAs designed in this work operate in class J [13] to achieve good linearity and efficiency simultaneously, as well as broadband. The starting point is biasing the transistor in deep class AB, therefore using a small current conduction angle to enhance efficiency. Another remarkable class J advantage is the flexibility in the PA design, since several combinations of the fundamental and second harmonic drain impedances are available in this class to achieve the desired RF performance. To determine these impedances, the easiest option is to use the intrinsic harmonic impedance values provided by (1) to (3):

$$Z_{f_0} = Ropt + j \cdot \alpha \cdot Ropt\ \Omega \tag{1}$$

$$Z_{2f_0} = -j \cdot \alpha \frac{3\pi}{8} Ropt\ \Omega \tag{2}$$

$$Z_{3f_0} = Z_{4f_0} = 0\ \Omega \tag{3}$$

where *Ropt* in this case, is the optimum intrinsic drain real impedance to operate in deep class AB, usually a compromise between output power and efficiency. This value can be obtained using load-pull, and α may vary from -1 to 1. Note that using $\alpha = 0$ is similar to operate in class B: the fundamental drain impedance is *Ropt* and the second harmonic impedance is a short circuit. The drain impedances configurations for $\alpha \neq 0$ causes the RF voltage time waveform to be shifted and boosted. Therefore, the efficiency remains the same as that achieved in class B. Using (1) to (3), the target intrinsic impedances at 2.45 GHz and 5.8 GHz, showed in Fig. 1 and Fig. 2, respectively, were calculated.

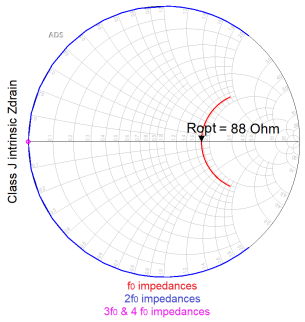

FIGURE 1. Class J intrinsic drain impedances at the lower frequency band.

B. SINGLE-BAND PA DESIGN

The single-band PAs were designed before the dual-band PA, to identify the expected RF performance at each band. Both single-band PAs bias networks use radial stubs (RF short circuits) in parallel to a $\frac{\lambda}{4}$ transmission line at the fundamental frequency, so that the fundamental signal be optimally delivered to the PA RF output. In addition, several parallel branches with series resistors and capacitors, filter low frequency spurious signals. Unconditional linear PA stability from low frequencies up to at least the second harmonic is achieved modifying these resistors values and including

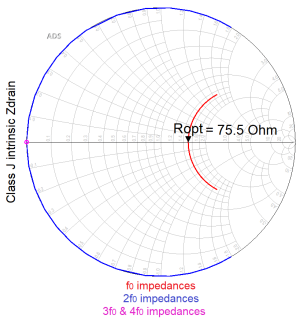

FIGURE 2. Class J intrinsic drain impedances at the higher frequency band.

a small series resistor at the gate RF terminal. Regarding the OMNs of both single-band PAs, they were designed to obtain the intrinsic class J impedances corresponding to $\alpha = 0.5$ for the lower band and $\alpha = 0.3$ for the upper band. These α values were determined by computing the intrinsic drain impedances (through access to the HEMT model internal nodes) while the extrinsic drain impedances (fundamental and second harmonic) were tuned/optimized. The RF output of each single-band PA are connected to stepped impedance filters to match the class J fundamental impedances. Furthermore, to aid matching the second harmonic output termination, a stub is used at the drain bias network, after the section filtering out the fundamental signal. The upper-band PA uses the technique in [14] to match fundamental and second harmonic impedances, independently. This method includes two $\frac{\lambda}{4}$ transmission lines for the second harmonic at the transistor's RF drain terminal, to avoid affecting the fundamental match, and an extra capacitor, whose selfresonant frequency is the second harmonic frequency, is included at the drain bias network, after the second harmonic matching. However, in this work the capacitor has been replaced with a radial stub, which is a short circuit at the second harmonic frequency, to avoid second harmonic signal being delivered to the dc drain source. With respect to the PAs input matching, also stepped impedance filters were used to achieve fundamental conjugate matching.

The layouts and the photographs of the single-band PAs. are shown in Figs. 3 and 4 for the 2.45 GHz class J PA and Figs. 5 and 6 for the 5.8 GHz class J PA. The simulated and measured results of the corresponding manufactured PA prototypes will be discussed in Section III.

C. DUAL-BAND PA DESIGN

The aim of this paper was the design of a dual-band PA without the need of reconfiguration, so the same circuit ensures good RF performance at both bands. Consequently, the bias networks are designed to enhance driving both fundamental signals to the RF output while properly biasing the transistor and aiding low frequency stability. For this purpose, we modified the bias network structure used in the single-band PAs (Section II-B) by using two radial stubs at both the drain and gate networks, instead

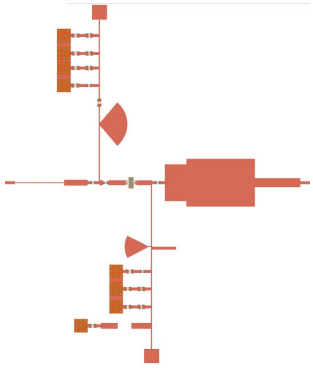

FIGURE 3. Single-band 2.45 GHz PA layout.

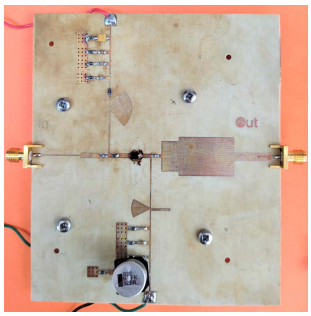

FIGURE 4. Single-band 2.45 GHz PA prototype photo. Size 10.6 cm × 12.4 cm.

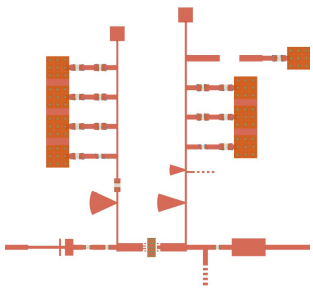

FIGURE 5. Single-band 5.8 GHz PA layout.

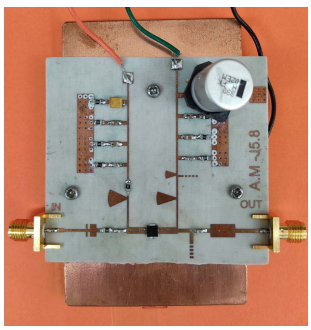

FIGURE 6. Single-band 5.8 GHz PA prototype photo. Size area of 6.3 cm × 5.8 cm.

of just one. An additional series resistor at the gate RF input was added to aid stability. To set the HEMT working in class J at each band, the intrinsic (through access to

TABLE 2. Dual-band PA intrinsic and extrinsic fundamental and second harmonic drain impedances before including matching networks.

Frequency [GHz]	$Zint_{f0}$ [Ω]	$Zint_{2f0}$ [Ω]	$Zext_{f0}$ [Ω]	$Zext_{2f0}$ [Ω]
2.45	90 - j60	4 + j80	10 - j18	1 + j2
5.8	88 - j76	0 + j37	12 - j31	80 + j80

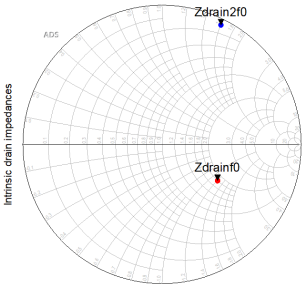

FIGURE 7. Target fundamental (red) and second harmonic (blue) intrinsic drain impedances before matching at 2.45 GHz.

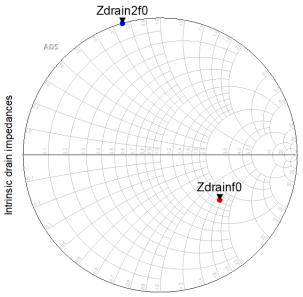

FIGURE 8. Target fundamental (red) and second harmonic (blue) intrinsic drain impedances before matching at 5.8 GHz.

the model internal nodes) and corresponding external output drain impedances are computed, obtaining the values included in Table 2. The intrinsic impedance values are also represented in Smith Charts at Figs. 7 and 8, for the lower and upper bands, respectively. These impedances correspond to $\alpha = -0.7$ for the lower band and, at the upper band, different α values were chosen for the fundamental ($\alpha = -1$) and the second harmonic impedances ($\alpha = -0.4$), since these values both provided good performance and were achievable within the constraints imposed by the bias network. Class J* was selected to aid matching, since using α values above 0 caused large differences between the obtained extrinsic drain impedances at both fundamental frequencies. These constraints did not allow using the same α values as in the single-band designs.

Next design steps involve designing the multiharmonic matching networks, starting with the OMN. Initially, the OMN is designed to match the fundamental frequency impedance at the upper band. The resulting network is shown in Fig. 9. To match second harmonic impedances, references [3] and [6] were considered. Those works added in the matching networks at the transistor's drain a $\frac{\lambda}{8}$ open stub

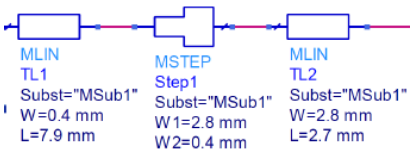

FIGURE 9. High-band fundamental frequency output matching network.

at f_0 to force a short circuit at $2f_0$ so in this work the same method is used but setting this stub initially at 5.8 GHz, prior optimization. Instead of applying the Two-Section Transmission Line (TSTL) used in [3] to achieve dual-band matching, we decided to perform a tuning process using the network, developed so far, but also adding an intermediate tapered line to give more design flexibility. The goal was to obtain a compromise between RF Pout and drain efficiency at the two bands of interest. The obtained OMN is shown in Fig. 10. Regarding the Input Matching Network (IMN), conjugate matching is applied, obtaining the fundamental source impedances $Z_s^{2.45GHz} = 170 - j33\Omega$ at the lower band and $Z_s^{5.8GHz} = 96 - j100\Omega$ at the higher band. A stepped impedance filter is again used to design the optimized IMN for the higher band, since at the lower band the expected RF performance of the dual-band PA is better. The final intrinsic drain impedance values are shown in table 3.

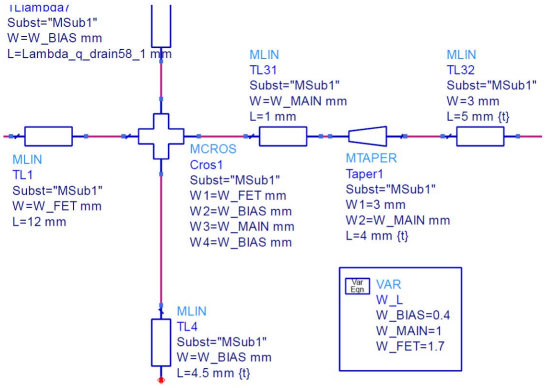

FIGURE 10. Dual-band OMN.

TABLE 3. Dual-band PA intrinsic fundamental and second harmonic drain impedances after including matching networks.

Frequency [GHz]	$Zint_{f0}$ [Ω]	$Zint_{2f0}$ [Ω]
2.45	73 - j0.3	11.5 + j1.7
5.8	50.2 - j20	2.6 + j20

These values are a compromise obtained by applying the proposed matching network architecture (which showed the best performance, despite limitations to fully provide the desired intrinsic harmonic impedances for the two separate bands) through an E-M optimization procedure to achieve drain impedances compatible with the B/J continuous and providing good performance. In particular, *Ropt* has varied

at both bands, as well as the α value, which corresponds with $\alpha \approx 0$ for the lower band and $\alpha \approx 0.25$ for the upper band.

The resulting layout and photograph of the dual-band PA prototype are included in Figs. 11 and 12.

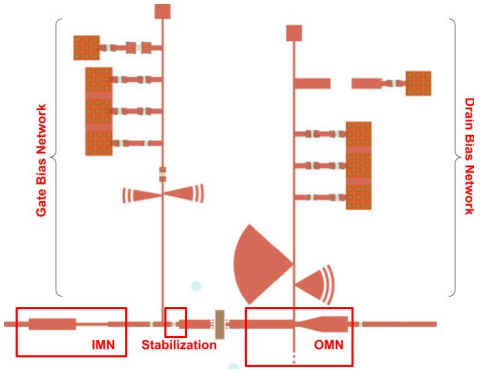

FIGURE 11. Dual-band PA layout.

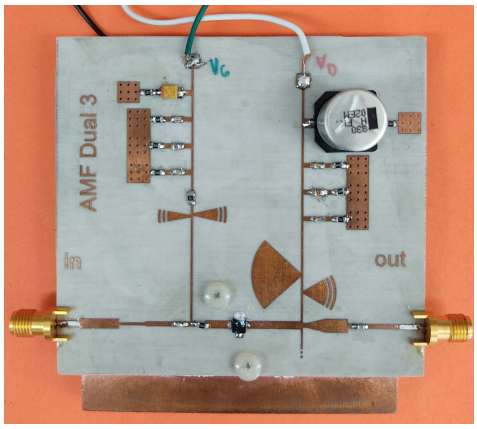

FIGURE 12. Dual-band 2.45 and 5.8 GHz PA prototype photo. Size area: 8.2 cm × 7.7 cm.

III. SIMULATED AND MEASURED RESULTS

The single-band and dual-band PAs PCBs (RO4003C) were processed at Cantabria University in Spain, using laser milling, and assembled in Vigo University (UVigo) on a copper heat-sink. Each PA was measured in UVigo laboratory under large and small signal excitation, using the set-up in Fig. 13, and a Vector Network Analyzer (VNA) (HP8510C), respectively. Regarding the measurements in large signal, a vector signal generator (E4438C ESG) and a driver amplifier are responsible of generating the PA RF input signal. The PA output is connected to a signal analyzer (N9000A CXA) through a directional coupler in order to attenuate the received signal. A dc power supply was used to bias the transistor.

A. SINGLE-BAND PAs MEASUREMENTS

The comparison between measured and simulated results can be observed in Fig. 14 (2.45 GHz single-band PA RF performance at 2.45 GHz) and Fig. 15 (5.8 GHz single-band PA RF

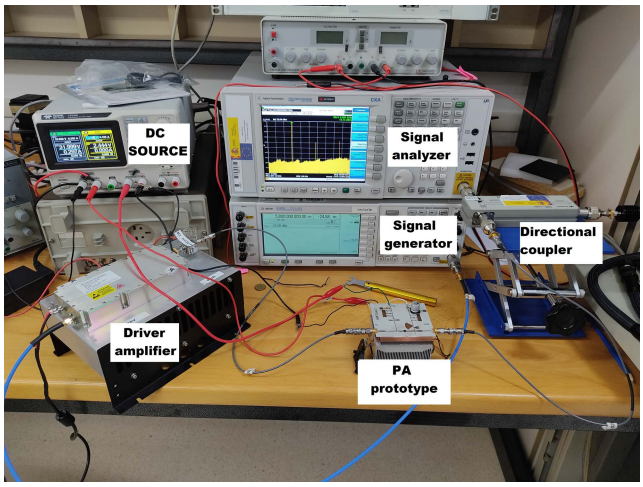

FIGURE 13. Set-up for the PAs prototypes large-signal characterization.

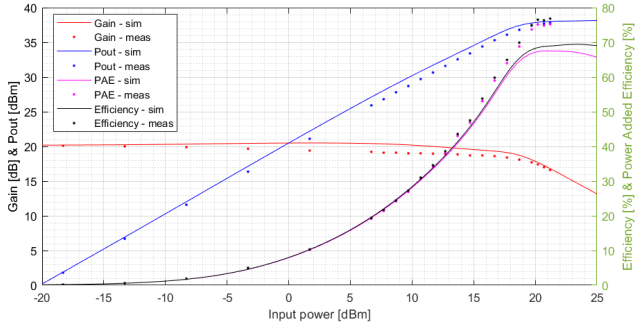

FIGURE 14. 2.45 GHz single-band class J PA, RF measured performance (dashed lines) vs. simulated one (continuous lines) at 2.45 GHz.

performance at 5.8 GHz). Whereas the simulations accurately predicted the low band prototype measurements, the 5.8 GHz class J PA predictions where less accurate, as expected. The 2.45 GHz single-band PA prototype provided at 2.45 GHz and 2dB compression, the measured performance of 18 dB of Transducer Power Gain (G_T), 36.8 dBm of Pout, 70% of Drain Efficiency (η) and 69% of PAE. At 3 dB compression, the RF Pout was 37.7 dBm, the η was 76.4% and the PAE was 75%. In the case of the 5.8 GHz single-band PA, at 5.8 GHz and 2 dB compression, the measured performance (without any post-fabrication tuning) was 11 dB of G_T, 34.5 dBm of RF Pout, 48.9% of η and 45% of PAE. At 3 dB compression, the Pout was 34.9 dBm, 48.3% of η and the PAE was 43.8%. This PA RF performance improved when the PA was measured at 5.6 GHz, as it is shown in Fig. 16.

Since previous high-band PA prototype showed a slight frequency shift, the dual-band PA was designed taking this problem into account.

B. DUAL-BAND PA MEASUREMENTS

The dual-band PA is measured at both bands separately, using the set-up in Fig. 13. The results at 2.45 GHz are shown in Fig. 17 and at the 2dB compression 14.8 dB of G_T, 35.7 dBm

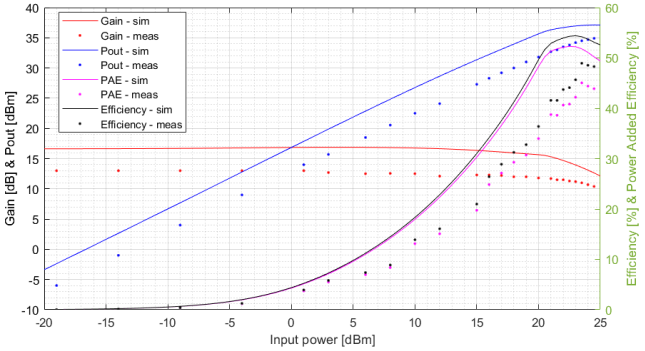

FIGURE 15. 5.8 GHz single-band class J PA, RF measured performance (dashed lines) vs. simulated one (continuous lines) at 5.8 GHz.

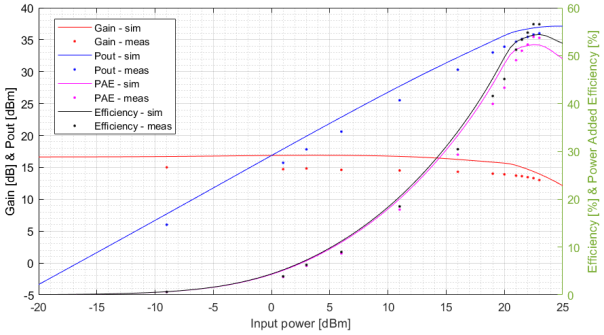

FIGURE 16. 5.8 GHz single-band class J PA, RF measured performance (dashed lines) vs. simulated one (continuous lines) at 5.6 GHz.

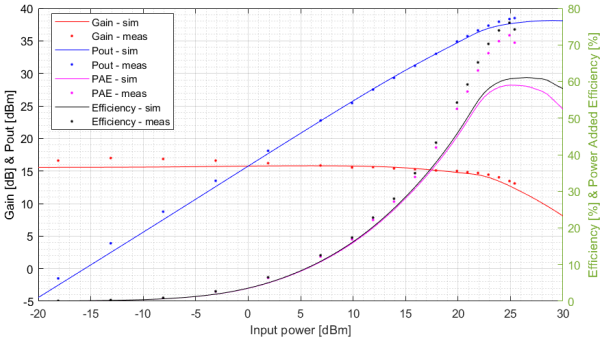

FIGURE 17. Dual-band class J PA, RF measured performance (dashed lines) vs. simulated one (continuous lines) at 2.45 GHz.

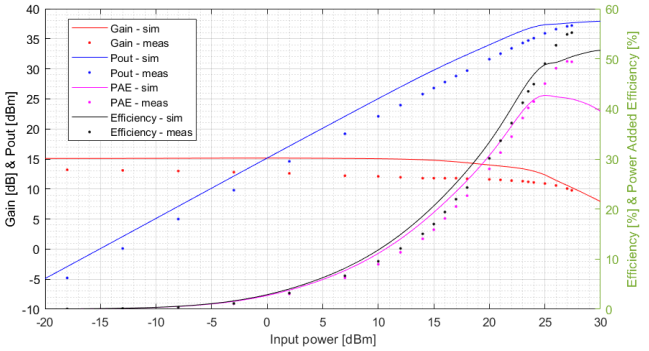

FIGURE 18. Dual-band class J PA, RF measured performance (dashed lines) vs. simulated one (continuous lines) at 5.8 GHz.

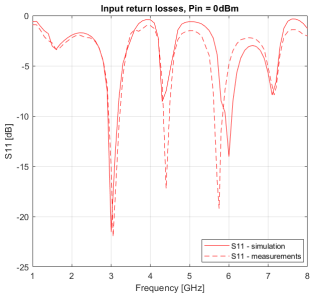

FIGURE 19. Dual-band PA simulated (continuous) vs. (dashed) measured S-parameters: input RL.

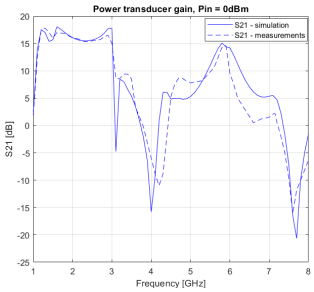

FIGURE 20. Dual-band PA simulated (continuous) vs. (dashed) measured S-parameters: G_T.

of Pout, 59.2% of η and 57.2% of PAE were obtained. It is observed that the measured PAE and drain efficiency at high compression levels improved over those values obtained in simulation. At 3dB compression, the measured RF output power shows similar results as the simulated one, reaching a Pout of 37.9 dBm, the η is 73.9% and the PAE is 71%.

At 5.8 GHz, the PA measurements at 2dB compression are 11.2 dB of G_T, 34.7 dBm of RF Pout, 43.5% of η and 40.2% of PAE. At 3dB compression the Pout is 37 dBm and regarding η and PAE we found similar behaviour at high compression levels than in the low band, reaching 55% of η and 50% of PAE. These results are shown in Fig. 18

The S parameters analysis of the dual-band PA performed comparing the simulations and the measurements with an VNA are shown in Figs.19 (input Return Losses (RL)) and 20 (G_T). The input RL show a frequency shift beyond 5 GHz. At 2.45 GHz they were not good, but they improved at 5.8 GHz to -12.8 dB, as expected from the way it was designed. As regards the S21 parameter, at 2.45 GHz a G_T of 15.4 dB is obtained and at 5.8 GHz, 14.3 dB. Broadband was achieved for the lower band, where 2 GHz of bandwidth were obtained. Whereas at the upper band, the bandwidth was 400 MHz, which is less than expected from simulations, but sufficient to work at the high ISM band selected in this work.

In tables 4 and 5, the simulated and measured RF results at 2dB compression and 3dB compression of the PAs

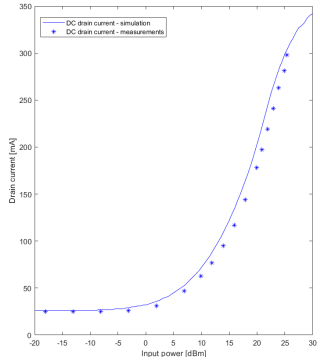

FIGURE 21. Dual-band PA simulated (continuous) vs. measured (stars) dc drain current. Fundamental frequency 2.45 GHz.

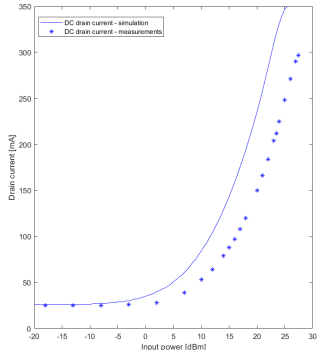

FIGURE 22. Dual-band PA simulated (continuous) vs. measured (stars) dc drain current. Fundamental frequency 5.8 GHz.

TABLE 4. This work simulated and measured PAs RF results at 2 dB compression.

PA / Frequency [GHz]	Simulation			Measurements		
	Gain [dB]	Pout [dBm]	η [%]	Gain [dB]	Pout [dBm]	η [%]
Single-band / 2.45	18.5	37.6	66.4	18	36.8	70
Single-band / 5.8	15	36.5	53.5	11	34.5	48.9
Dual-band / 2.45	13.7	37.2	59.3	14.8	35.7	59.2
Dual-band / 5.8	13.2	36.7	45.5	11.2	34.8	43.5

TABLE 5. This work simulated and measured PAs RF results at 3 dB compression.

PA / Frequency [GHz]	Simulation			Measurements		
	Gain [dB]	Pout [dBm]	η [%]	Gain [dB]	Pout [dBm]	η [%]
Single-band / 2.45	17.5	37.9	68.8	17	37.7	76.4
Single-band / 5.8	14	37	54.4	10	34.9	48.3
Dual-band / 2.45	12.7	37.7	60.7	14	37.9	73.9
Dual-band / 5.8	12	37.4	49.1	10.1	37	55

included in this work, respectively, are presented. Except for the single-band PA at 5.8 GHz, the rest of the PAs show higher η and PAE results at high compression levels in comparison with simulated ones. Differences in selfbiasing behaviour at high powers, possible due to difficulties in the prediction of the HEMT nonlinear distortion, especially at high frequencies, and the heat sink induced thermal response, are probably responsible of significant differences between the simulated and measured dc drain current (see Figs.21 and 22), hence affecting the efficiency results. In addition, at high power levels in some instances the measured RF Pout exceeds the simulated one, thus contributing to more disagreements in the final efficiency.

IV. CONCLUSION

This work describes the design of a hybrid GaN dual-band class J* PA at two ISM bands, whose center frequencies are 2.45 and 5.8 GHz, suitable for UAVs communications. A prior approximation of the expected dual-band PA performance was obtained by designing and manufacturing two single-band PAs at the center frequencies of each band. At 2dB compression the dual-band PA prototype supplies 35.7 dBm and 34.8 dBm of RF Pout at the lower and upper band, respectively, and 59.2% and 43.5% of η, whereas at 3 dB compression, 37.9 dBm of Pout are obtained at the low band and 37 dBm at the upper band, as well as 73.9% and 55% of η. The measured results are consistent with simulations. As far as we know, no dual-band PAs prototypes providing similar measured RF performance at the same bands are found in the literature.

ACKNOWLEDGMENT

The authors would like to thank Modelithics Inc., Tampa FL, USA, for providing component models (under the University License Program), to Cantabria University, Spain, for PCB processing by laser milling and to Ignacio Boubeta, at atlanTTic Research Center, for his aid in assembling the PA prototypes heat sinks.

REFERENCES

[1] R. Liu, D. Schreurs, W. De Raedt, F. Vanaverbeke, and R. Mertens, "Concurrent dual-band power amplifier with different operation modes," in *IEEE MTT-S Int. Microw. Symp. Dig.*, Jun. 2011, pp. 1–4, doi: 10.1109/MWSYM.2011.5972698.

[2] P. Wright, J. Lees, J. Benedikt, P. J. Tasker, and S. C. Cripps, "A methodology for realizing high efficiency class-J in a linear and broadband PA," *IEEE Trans. Microw. Theory Techn.*, vol. 57, no. 12, pp. 3196–3204, Dec. 2009, doi: 10.1109/TMTT.2009.2033295.

[3] H. Cai, L. Mao, J. Cong, and Y. Zhang, "Design of a dual-band high efficiency class-J power amplifier," in *Proc. 9th Int. Conf. Adv. Infocomm Technol. (ICAIT)*, Nov. 2017, pp. 75–79, doi: 10.1109/ICAIT.2017.8388892.

[4] K. Niotaki, M. J. Cañavate-Sánchez, A. Collado, G. Goussetis, A. Georgiadis, and T. Brazil, "2.45 GHz/5.8 GHz dual-band power amplifier for wireless power transfer in space applications," in *Proc. Conf. Active Passive RF Devices*, London, U.K., 2017, pp. 1–4, doi: 10.1049/ic.2017.0006.

[5] A. Atanaskovic, A. Doric, B. Alorda, and N. Males-Ilic, "Dual band power amplifier linearization," in *Proc. 14th Int. Conf. Adv. Technol., Syst. Services Telecommun. (TELSIKS)*, Oct. 2019, pp. 37–40, doi: 10.1109/TELSIKS46999.2019.9002122.

[6] M. Shariatifar, M. Jalali, and A. Abdipour, "Design of a high-efficiency dual-band class-J/J power amplifier considering concurrent-mode input drive," *Int. J. RF Microw. Comput.-Aided Eng.*, vol. 30, no. 3, Mar. 2020, Art. no. e22064, doi: 10.1002/mmce.22064.

[7] Q. Xiao, L. Chen, W. Lu, and C. Zhu, "A dual-band PA for counter UAV applications," in *Proc. Int. Symp. Comput. Technol. Inf. Sci. (ISCTIS)*, Jun. 2021, pp. 134–137, doi: 10.1109/ISCTIS51085.2021.00035.
[8] R. Fagotti, A. Cidronali, and G. Manes, "Concurrent hex-band GaN power amplifier for wireless communication systems," *IEEE Microw. Wireless Compon. Lett.*, vol. 21, no. 2, pp. 89–91, Feb. 2011, doi: 10.1109/LMWC.2010.2098859.
[9] H. Zhao and D. Zhang, "Dual-band class-F power amplifier with bandwidth expansion based on sector microstrip branch for 5G applications," *IEEE Microw. Wireless Compon. Lett.*, vol. 31, no. 7, pp. 877–880, Jul. 2021, doi: 10.1109/LMWC.2021.3074411.
[10] Z.-B. Zhang, L.-Y. Wei, and F.-C. Chen, "A dual-band high-efficiency power amplifier based on novel impedance matching and harmonic control structure," in *Proc. Cross Strait Radio Sci. Wireless Technol. Conf. (CSRSWTC)*, Oct. 2021, pp. 275–277, doi: 10.1109/CSRSWTC52801.2021.9631577.
[11] P. Zurek, T. Cappello, and Z. Popovic, "A concurrent 2.2/3.9-GHz dual-band GaN power amplifier," in *Proc. IEEE Topical Conf. RF/Microw. Power Modeling Radio Wireless Appl. (PAWR)*, Jan. 2019, pp. 1–4, doi: 10.1109/PAWR.2019.8708730.
[12] Z. Zhang, Z. Cheng, V. Fusco, and C. Gu, "Design of a dual-band power amplifier using a simple method," *IEEE Microw. Wireless Compon. Lett.*, vol. 31, no. 2, pp. 149–152, Feb. 2021, doi: 10.1109/LMWC.2020.3047733.
[13] S. C. Cripps, P. J. Tasker, A. L. Clarke, J. Lees, and J. Benedikt, "On the continuity of high efficiency modes in linear RF power amplifiers," *IEEE Microw. Wireless Compon. Lett.*, vol. 19, no. 10, pp. 665–667, Oct. 2009, doi: 10.1109/LMWC.2009.2029754.
[14] Y. Park, D. Minn, S. Kim, J. Moon, and B. Kim, "A highly efficient power amplifier at 5.8 GHz using independent harmonic control," *IEEE Microw. Wireless Compon. Lett.*, vol. 27, no. 1, pp. 76–78, Jan. 2017, doi: 10.1109/LMWC.2016.2630853.

AINHOA MORALES-FERNANDEZ was born in Zürich, Switzerland, in 1996. She received the B.S. and M.S. degrees in telecommunication engineering from the Universidade de Vigo (University of Vigo, UVigo), Spain, in 2021, where she is currently pursuing the Ph.D. degree in communications engineering, specializing in electronics for communications.

In 2018, she was an Intern with the atlanTTic Research Center for Telecommunication Technologies, Vigo, where she received advanced formation in hybrid power amplifiers' design in microstrip technology. Since 2020, she has been a Research Assistant at the AtlanTTic Research Center. Her research interests include nonlinear device modeling and microwave circuit design.

MONICA FERNANDEZ-BARCIELA (Senior Member, IEEE) received the M.Sc. degree in physics (electronics) from the University of Santiago de Compostela (USC), Spain, in 1989, and the Ph.D. degree in communications engineering from the University of Vigo (UVigo), Spain, in 1996. Her thesis research work was partly performed at the Fraunhofer-Institut (IAF), Germany, through different stay grants. She joined the UVigo Communications Technologies Department, in 1990, first as a FPI granted Ph.D. student, later as an Assistant Professor (1991) and an Associate Professor (1997) at the Vigo School of Communication Engineering. From July 2010 to September 2014, she was the Vice-Director of the Signal Theory and Communications Department, UVigo. From December 2017 to December 2019, she was the President of the IEEE Spanish Joint Chapter AP003/MTT017. Her main research work has been related to active device nonlinear black-box modeling, device characterization, and circuit design for communications applications.

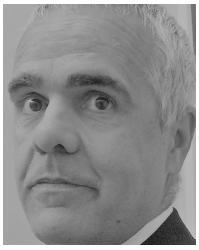

FERNANDO ISASI-VICENTE received the master's degree in communications engineering from the Politechnic University of Madrid, Madrid, Spain, in 1990, and the Ph.D. degree from the University of Vigo, Vigo, Spain, in 1998.

He joined the University of Vigo, as an Assistant Professor, in 1993. He is currently an Associate Professor at the Vigo's Communication Engineering School, Vigo. His main research work has been related to cellular networks and wireless communications. He has published research papers in international journals and conferences and leaded many contracts with industry. He is a member of the Spanish Association of Communication Engineers.

FERNANDO MARTIN-RODRIGUEZ received the degree and Ph.D. degrees in communications engineering from the University of Vigo, Vigo, Spain, in 1993 and 1999, respectively.

He joined the University of Vigo, as an Assistant Professor, in 1995 (formerly, a Lecturer at the Computer Science School, University of La Coruña). He is currently an Associate Professor at the Vigo's Communications Engineering School, Vigo. His main research work has been done in image analysis and computer vision, data, and wireless networks. He has published research papers in journals and conferences, and leaded contracts and research projects, directed a Ph.D. Thesis. He is a member of the Spanish and Galician Association of Communication Engineering Institution who awarded him with the "Better ITC Project With Social Consciousness" Prize in 2018. He was a recipient of a Fellowship to research at the NIST, Gaythersburg, MD, USA, in 1997.

PAUL J. TASKER (Fellow, IEEE) led a research position with Cornell, WI, USA, from 1983 to 1990, establishing HFETs as the technology of choice for high frequency applications. His collaboration with general electric led to the first use of HFET technology in radio telescopes used by NRAO to receive transmissions from NASA's Voyager 2. From 1990 to 1995, he directed the GaAs monolithic microwave integrated circuit (MMIC) technology development with the Fraunhofer Institute (IAF), Freiburg, Germany, delivering state-of-the-art 60–100 GHz GaAs MMICs. In 1995, joined Cardiff University (U.K.), establishing the Centre for High-Frequency Engineering (CHFE), in 1996. The CHFE is now recognized internationally for its pioneering work in developing waveform engineering concepts and their application to microwave and millimeter-wave power amplifier (PA) design. He has more than 30 years of experience in design, fabrication, characterization, and modeling of high frequency devices. He is involved in collaborative projects with a wide range of academic and industrial partners. He was a Distinguished Microwave Lecturer with the IEEE MTT Society from 2008 to 2010.